ORIGINAL PAPER

Investigating the Influence of Friction and Material Wear on Triboelectric Charge Transfer in Metal–Polymer Contacts

J. L. Armitage[1] · A. Ghanbarzadeh[1] · M. G. Bryant[1] · A. Neville[1]

Abstract

A reciprocating tribometer has been modified with a high-impedance electronic measurement circuit for the purpose of addressing the question of how tribology influences triboelectric charging. This measurement circuit allows for the accurate measurement of potential difference, induced current, and total triboelectric charge generated within the tribometer contact. These electronic properties can now be effectively compared with tribological parameters such as contact force, relative sample velocity, and friction coefficient (μ) for varying contacts. In this study we present our apparatus, alongside our findings regarding the influence of material wear mechanisms and friction on the accumulation and dissipation of triboelectric contact charges.

Keywords Triboelectric nanogenerator · Contact electrification · Polymer wear · Polymer tribology

1 Introduction

One particularly overlooked phenomenon in tribology is that of frictional electrification—otherwise referred to as the triboelectric effect, contact electrification, or triboelectric charging [1]. The triboelectric effect is described as the transfer of electronic charge between two bodies in physical contact [1]. These bodies can take various forms in terms of state and composition, and examples of triboelectric charge transfer between solids [2], liquids [3], and gases [4] are prominent in everyday life. The effects of triboelectric charging are evident in a multitude of engineering applications. The 'clumping' of pharmaceutical powders in powder handling systems is attributed to the triboelectric transfer of electrostatic charge between the particles of powder and the surfaces they contact [5]. Fuel transfer systems are also suitably grounded as a way of inhibiting the triboelectric build-up of static charge within the fuel as it flows across a particular substrate surface [6]. 'Precipitation static' is also an important phenomenon to consider in aviation, since static charges build up on aircraft fuselages as they contact rain, snow, ice, or dust particles—via triboelectric charging [7]. Despite the implications of triboelectric charging in

many engineering applications, the potential for it to be utilised in the fields of energy recycling [8] and self-powered sensing [9] highlights its importance in many potential scientific and technological areas. Various forms of triboelectric nanogenerator (TENG) have been proposed and developed as solutions for converting otherwise wasted kinetic energy into electrical energy [10]. TENGs achieve this form of energy harvesting via the electrostatic induction of the charges which are generated through triboelectric charging within the device [11].

Much research has been conducted on the construction of TENG devices [12], as well as on the underlying mechanisms of contact electrification [1], but the role of tribology in triboelectric charging remains in need of further investigation. The majority of current research into triboelectric charging is conducted on contacts that involve zero lateral relative motion [13], meaning that identifying the role of friction in triboelectric charging remains a long-standing enigma. The longevity of TENG devices is also rarely questioned in existing research, which is a factor that should be considered in the context of material wear in tribological contacts.

1.1 The Triboelectric Effect: An Overview of Current Theory

The electron has previously been identified as the primary charge carrier for triboelectric charging between solid surfaces [14], although mechanisms for ion transport have been proposed for specific circumstances such as within corrosive

✉ J. L. Armitage
py12ja@leeds.ac.uk

[1] Institute of Functional Surfaces (iFS), School of Mechanical Engineering, University of Leeds, Woodhouse Ln, Leeds LS2 9JT, UK

environments [15]. Within this article, the term 'triboelectric charge transfer' will be used to solely describe the transfer of electrons via triboelectric charging unless otherwise stated.

An important prerequisite for triboelectric charge generation to occur between two bodies is having differing electronic surface structures [14]. In the case of two contacting materials with identical electronic surface structures, triboelectric transfer will only occur as a way of redistributing any pre-existing surface charges on either surface to attain an equilibrium state [16]. The mechanism for triboelectric charge transfer is a thermodynamic process, where electrons travel from the highest occupied energy states of one 'donor' surface into the lower unoccupied states of the 'acceptor' counter-surface [17].

When two surfaces of differing electronic structures are brought into contact, a contact potential difference (CPD) is formed at the interface [4]. This CPD is proportional to the difference in energy between the aforementioned surface states, as well as their respective state degeneracies [18]. The CPD then drives the transfer of electrons, via mechanisms such as quantum tunnelling, across the interface to restore local thermodynamic equilibrium. When conductive materials are in contact, the difference between their respective work functions is viewed as the driving force behind triboelectric charge transfer [19]. The more complex case, considering insulating materials, is often simplified by assigning such insulating materials with 'effective' work functions situated within their respective energy band gaps [20]. These effective work functions for semi-conductors and insulating materials are often measured using ultraviolet photoelectron spectroscopy (UVPES) [21] or through kelvin probe force microscopy (KPFM) [22]. A graphical representation of this electron transfer mechanism is depicted in Fig. 1, stating the case for a conductor–insulator contact and an insulator–insulator contact, respectively.

Once transferred across a contact interface, any electrons transported to an insulating surface are assumed to become isolated to their new surface state and form a quasi-capacitive layer [14]. Through this isolation of transferred charge, two insulating surfaces in contact accumulate equal yet opposing static charges. The polarity and magnitude of charge accumulated on a surface via triboelectric charging is dependent on its electronic structure relative to the counter-surface involved [14] as well as the tribological parameters that describe the form of contact.

1.2 Overview: Triboelectric Nanogenerators

Triboelectric nanogenerators (TENGs) are a group of devices that were initially proposed in 2012 [10] as a solution for recycling otherwise wasted mechanical energy into a useful electro-motive force. The primary mechanism behind their operation is the electrostatic induction of a conduction current, driven by a time-varying electric field—commonly referred to as a displacement current—that is generated through the relative movement of charges that are generated via triboelectric charging [9]. A visual representation of this mechanism for generating this time-varying potential difference and resulting current is shown in Fig. 2a and b, respectively. The high-impedance nature of TENG devices means that they generally produce electrical outputs that contrast with electromagnetic generators, resulting in high voltages (up to the order of kV) and low currents (often in the order of μA) [24]. The principle of electrostatic induction allows for a great deal of flexibility in terms of device construction and configuration and forms the basis of our methodology for measuring triboelectric charge.

TENG devices utilise many forms of mechanical interaction [25], including but not limited to contact-separation, lateral sliding [26], and the flowing of fluids across a substrate surface [27]. It is therefore clear that tribology plays a pivotal role in the operation of TENGs. Much research has been conducted on TENG devices with a view to optimising their performance and expanding their capabilities [12]. This research also includes investigations into the fundamentals of

Fig. 1 Depicting the transference of charge between a metal and an insulator (**a**), and the transference of charge between two insulators (**b**) in accordance with molecular ion-state theory [17]. The Fermi level and effective Fermi levels are denoted by E_{Fn} and E_{Fn}, respectively. Fermi–Dirac energy distributions are described by $f_n(E)$ and state densities are described by $\rho_n(E)$ with A and D denoting acceptor and donator states, respectively. Figure sourced with permission from [23]
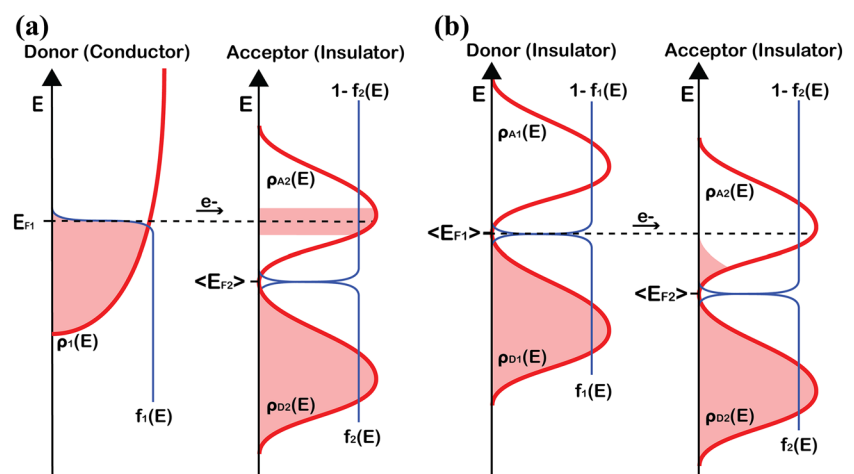
Fig. 2 Depicting the operation of a TENG device which utilises the reciprocating movement of an insulating surface laterally across two conductive counter-surfaces (abbreviated as SF-TENG) where the external circuit is described as **a** having an infinite resistance (open-circuit) and **b** zero resistance (short-circuit, right). Grey blocks denote a conductive material whereas red blocks denote an electronegative insulator. **c** A graphical representation of how a stereotypical DSF-TENG electrical output would couple with its friction response
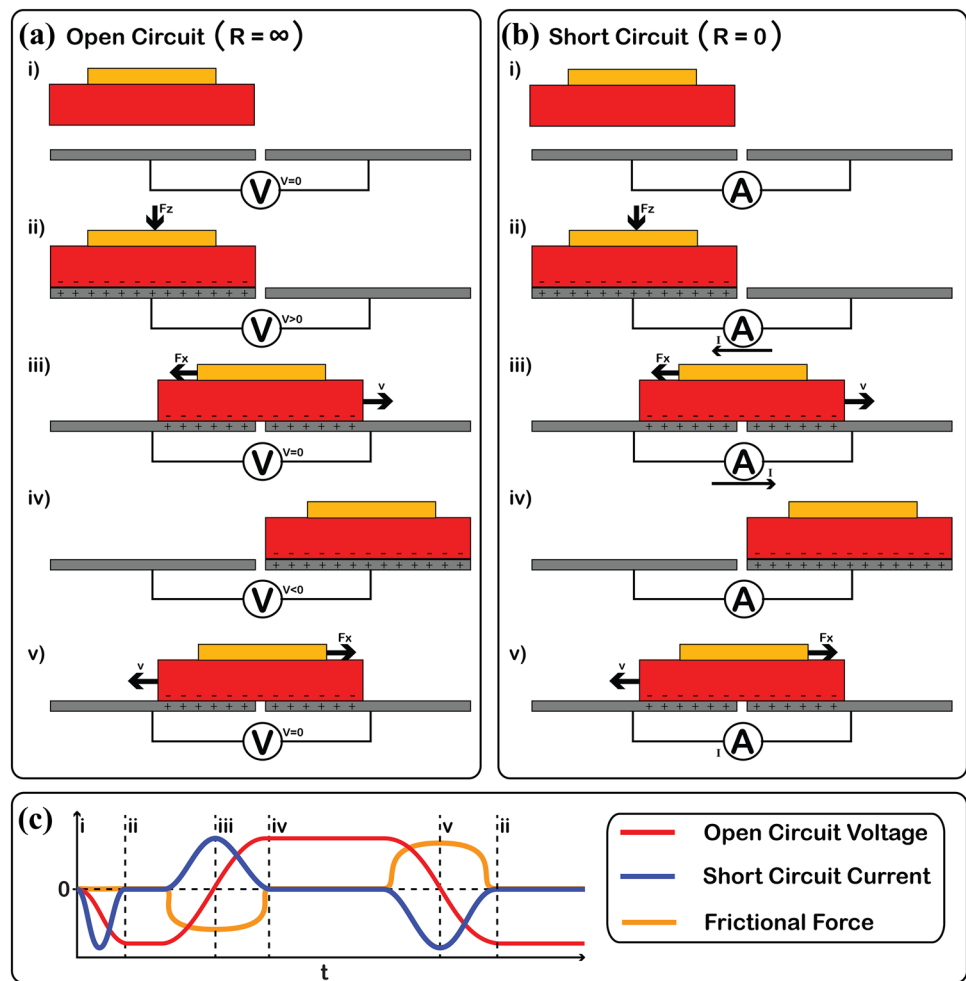
static contact electrification using atomic force microscopy, and how parameters such as temperature affect this form of triboelectric charging [1]. The role of tribology in the context of TENG applications, however, is often overlooked.

The largest problem that remains in the field is the contribution of dynamic friction to triboelectric charging. Previous research has suggested that the mechanism for initiating triboelectric charge transfer is highly dependent on electron–phonon interactions within the donor surface [28]. Phonon packets are also known to be produced by friction and other mechanical interactions [29], but a theory as to how these two mechanisms interact is yet to be proposed. The influence of localised contact pressure on triboelectric charge transfer is also in need of further discussion. Previous research has shown that triboelectric charge transfer is only possible between two strongly overlapping electron wave functions [14], meaning that localised contact pressure may have a strong influence on the amount of charge transferred between two contacting asperities. Another problem that arises when tribology is considered is that of material wear. This is often seen as negligible in TENG literature since most research has been conducted on contact-separation based TENG devices where no sheer

stress is applied and under low nominal contact pressures [30]. However, with soft materials such as polymers seeing such prominent use in TENG applications, it is difficult to prevent even the smallest amount of material wear from interfering with the triboelectric charge accumulation process.

The purpose of this study is to provide a means of tribological investigation, focussed on correlating tribological parameters to triboelectric charge transfer. This will provide an invaluable insight into the underlying mechanisms of triboelectric charging and how they scale to applications. In turn, this insight may also provide ways to enhance and prolong the performance of TENG devices. Replicating a triboelectric nanogenerator within a tribometer environment is the most logical approach towards achieving this understanding.

2 Apparatus and Methodology

A Bruker Universal Mechanical Tester TriboLab tribometer (UMT) has been modified to accommodate various forms of triboelectric nanogenerator. These modifications include new insulating plate-on-plate sample holders, allowing for the

geometry of TENG contacts to be replicated within the tribometer, as well as the integration of two Keithley 6517B/E electrometers into the data acquisition unit of the UMT for high-impedance electronic measurements. A full schematic of the UMT-TENG apparatus is given in Fig. 3a.
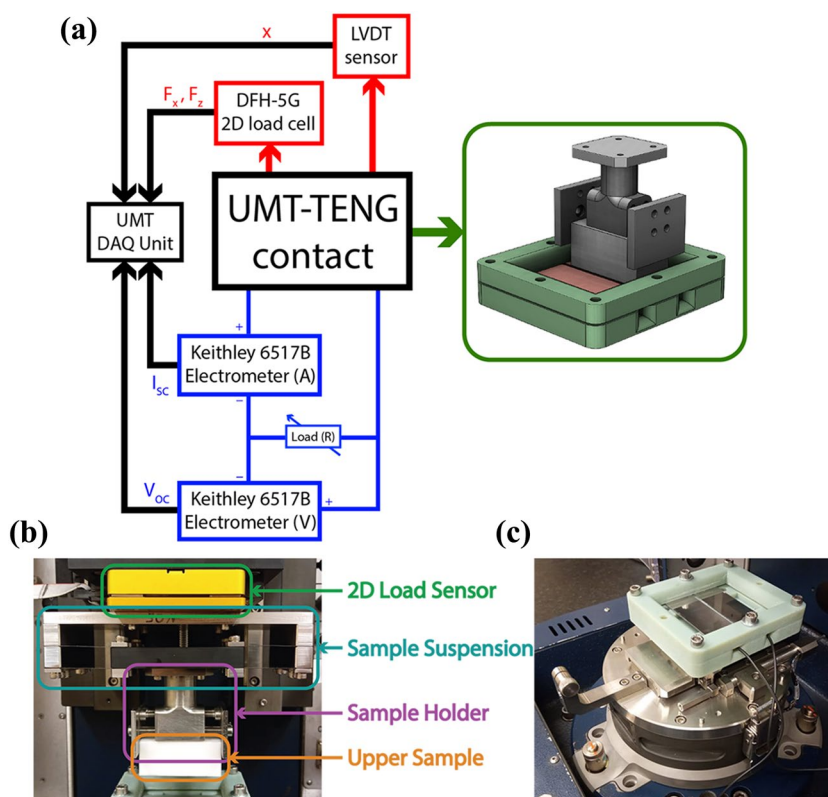
2.1 The UMT-TENG Contact

The specific device geometry being replicated for this study is that of a dielectric sliding-freestanding-layer TENG (DSF-TENG). This form of TENG contact comprises of an insulating upper sample being reciprocated across the surface of two conductive lower samples. This configuration of sliding-mode TENG is the easiest to accommodate within a reciprocating tribometer as it allows for the consistent measurement of friction under a constant applied load throughout the full range of movement of the device. The two conducting samples in this arrangement may also have a thin insulating coating, separating them from direct contact with the insulating upper sample. A side-on visual representation of a DSF-TENG contact is given in Fig. 2. The contact geometry for the majority of previously tested TENG devices is plate-on-plate, with contact sizes in the order of several cm^2 [12]. This is to provide a large enough contact area for an accurately measureable amount of charge to be generated for most conventional material pairings, in the order or several tens of nC.

An insulating sample holder was additively manufactured in an acrylonitrile–butadiene–styrene copolymer (ABS) to accommodate the conductive elements of the DSF-TENG contact without any leakage of charge to the surrounding environment. 3D representations of the DSF-TENG contact within the UMT-TENG sample holders is given in Fig. 3. The upper sample holder, machined from stainless steel, was designed to attach to the UMT's upper sample suspension and can also accommodate insulated samples of varying sizes. An image of this arrangement is given in Fig. 3b. The UMT-TENG apparatus also allows for the testing of other laterally sliding TENG modes such as attached-electrode and single-electrode devices [13]. Non-contact testing is also accommodated by this apparatus as a way of measuring the dissipation of electrostatic charge from insulating surfaces.

2.2 Tribological Measurements

The reciprocating drive of the UMT was used to move the lower conductive samples relative to the upper insulating sample and is shown in Fig. 3c. The mechanism controlling this motion is a form of reverse-piston, where the rotational motion of the UMT motor is translated to a reciprocating motion via an adjustable piston rod. This gives the relative movement of the samples a sinusoidal velocity profile, where the largest velocities are observed in the middle of the stroke.

Fig. 3 **a** Schematic representation of the full UMT-TENG testing apparatus (left) accompanied by a 3D model of the assembled UMT-TENG contact itself (right). Elements highlighted in blue represent elements that constitute the electronic measurement circuit, whereas elements highlighted in red contribute to tribological measurements. **b** Photograph of the UMT-TENG upper sample holder assembly. **c** Image of the UMT's reciprocating drive module with the UMT-TENG lower sample holder attached.

A vertical force (F_z) is applied to the UMT-TENG contact as the upper sample is lowered via a screw-driven linear actuator. As the upper and lower samples are moved relative to each other by the reciprocating drive whilst in contact, frictional resistance works to impede this movement. The friction coefficient for a mechanical contact (μ) is given as the force imparted by friction (F_x) divided by F_z.

$$\mu = \frac{F_x}{F_z} \tag{1}$$

A two-dimensional force sensor connected to the upper sample is used to measure both F_z and F_x during testing. A suspension system is also affixed between the upper sample and sensor to mitigate any acoustic vibrations and protect the load cell from potential damage. The force sensor gives precise measurement of and control over the applied load with a resolution of 2.5 mN. This allows for the correlation of friction data with the electrical output of the contact. A linear variable differential transformer (LVDT) sensor is also used to accurately measure the relative position of the samples over time ($x(t)$). This allows for the plotting of friction, output current, and output voltage over both time and relative sample position. Being able to plot the electrical output of the TENG contact over relative sample position also allows for the influence of system geometry to be investigated in greater detail and determine which existing models are able to predict TENG outputs most accurately.

2.3 Electronic Measurement Circuit

Two Keithley 6517B/E electrometers were integrated with the data acquisition unit of the UMT and attached to the conductive elements of the DSF-TENG contact within the tribometer. These electrometers allow for the accurate measurement of the outputs from high-impedance electronic applications such as TENGs. Both electrometers are utilised in varying configurations for the analysis of different UMT-TENG output characteristics. Before fully describing the involvement of these electrometers, a more detailed description of the DSF-TENG contact within the UMT is required for clarity. When triboelectric charging occurs within a DSF-TENG contact, electrostatic charges accumulate on the insulating surface within the contact. These charges induce mirror charges within the conductive counter-surfaces due to the Coulomb force. As the upper sample is reciprocated across the two lower conductive surfaces, these mirror charges move to match its location. If the two lower samples are electronically connected with no impedance, a 'short-circuit' current (I_{SC}) would be measured passing between them as the upper sample moves to represent the induced movement of mirror charges. The higher the relative velocity of the upper and lower samples, the higher this induced current. A visual representation of the case for

measurement of both μ and I_{SC} over time and relative sample position is given in Fig. 2b.

If a voltmeter (theoretically, each with an infinite internal resistance) is connected to each of the two lower samples, both connected via a common ground, an oscillating 'open-circuit' voltage (V_{OC}) would be measured as the difference between the two voltmeter readings [31, 32]. This V_{OC} would correlate with the relative position of the upper and lower samples. Physically the potential difference between the two lower samples would reach a maximum when the upper sample reaches either end of its stroke, as a result of the distance dependent electric field (DDEF) produced by the trapped tribocharges on the insulator surface [33]. An accurate depiction of both short-circuit and open-circuit operating modes is given in Fig. 2. The characteristics of both I_{SC} and V_{OC} are influenced by the geometry of the device, e.g. the lateral spacing of the lower samples. Both electrometers are utilised simultaneously alongside a variable resistor to accommodate electrical output testing with various external impedances. The schematic for this circuit arrangement is given in Fig. 4.

2.4 Sample Preparation

The geometry of the DSF-TENG contact requires one upper insulating sample and two lower conductive samples for each test. To avoid any complications in the modelling of this device, the two lower samples for each test are composed of the same conductive material. To maximise the efficiency of the device whilst retaining a simple device construction, the lateral length of the upper and lower samples should be equal to the stroke length minus the lateral spacing between the lower samples. This is in order to maximise the apparent contact area between the upper and respective lower sample at either end of the reciprocating stroke. The stroke length of the UMT reciprocating drive is set at its maximum of 25 mm for the purpose of UMT-TENG testing, and the lateral spacing is kept to a relatively small 2 mm to maximise the apparent area of contact within the apparatus. The widths of the upper and lower samples perpendicular to the stroke length whilst parallel to the plane of contact are 50 mm and 70 mm, respectively. The higher width of the lower samples is purely to accommodate them within the clamping mechanism of the lower sample holder. The lower conductive samples were cut from 2 mm thin sheets of their respective metals. The thickness of the upper samples is set at 25 mm for ease of construction and ease of accommodation within the upper sample holder.

Three different polymers were used as material choices for upper sample composition: Polytetrafluoroethylene (PTFE, Teflon), Poly(hexamethylene adipamide) (PA66, Nylon 66), and Polyoxymethylene (POM, Delrin). These three polymers were chosen as they have seen prominent use in early TENG contacts, owing to their differing molecular electronic structures [2]. Two different metals were also used as material
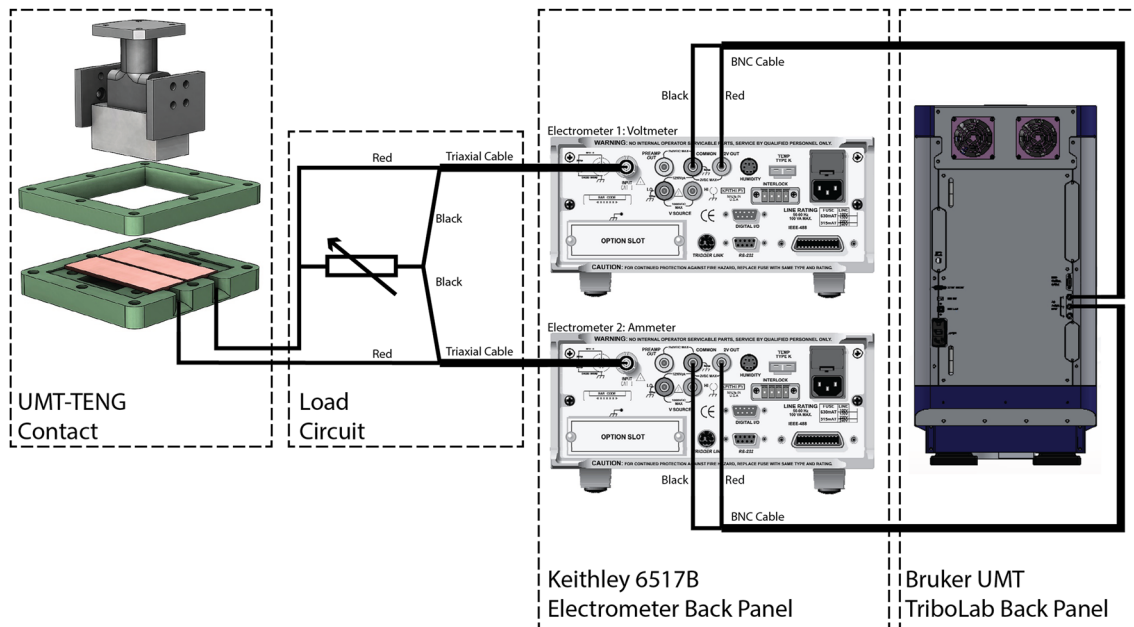
Fig. 4 Wiring schematic of the UMT-TENG apparatus set-up. Indicating the exact connections used to integrate the Keithley 6517B electrometers with the data acquisition unit of the UMT. Please note that the BNC ports on the back panel of the UMT have been internally connected to pins 15 and 16 of junction 15 on the UMT data acquisition unit

choices for the lower samples: an Aluminium–Scandium alloy, and Stainless Steel (UNS S31603). The work functions of Aluminium and Stainless steel are given as 4.26 eV [34] and 4.30 eV [35], respectively, which are both comparatively lower than most metals. The mechanical properties of both metals differ substantially, where stainless steels have a higher density and higher mechanical moduli than aluminium alloys [36]. The mechanical properties of all materials used in this study are given in Table 1.

The polymer samples were also given differing surface texture parameters to investigate the influence of both material composition and surface texture on triboelectric charge transfer within a controlled environment. 180 grit silicon carbide grinding pads were implemented to increase the mean arithmetic roughness (R_a) of some samples of each polymer. The metal counter-surfaces and remaining polymer surfaces were polished to a mirror-like texture using a diamond suspension to minimise the influence of counter-surface topography and to simplify any future modelling of the contact.

2.5 Testing Procedure

A series of reciprocating tests using the UMT-TENG apparatus has been conducted to investigate the influence of sliding friction and material wear on triboelectric charging. Each test has been designed to replicate the operation of a DSF-TENG contact, consisting of differing material combinations and under varying tribological parameters. Testing was conducted under applied loads of both 5 N and 10 N to investigate the influence of contact force on triboelectric charge transfer. The reciprocating stroke length was set to its maximum of 25 mm and a reciprocating frequency of 2.5 Hz was used for tribological

Table 1 Mechanical properties for all sample materials used in UMT-TENG testing

Material	Elastic modulus (GPa)	Shear modulus (GPa)	Hardness (Rockwell)	Poisson's Ratio	Work function (eV)
Stainless Steel	193 [36]	77.2 [41]	79 (B) [41]	0.25 [36]	4.30 [35]
Aluminium	68.9 [37]	27 [43]	60 (B) [43]	0.33 [37]	4.26 [34]
Delrin	3.15[a]	0.915[a]	93 (R)[a]	0.37[a]	–
Nylon 6-6	1.85[a]	1.15[a]	115 (R)[a]	0.42[a]	4.20 [38][b], 5.61 [39][b]
Teflon	0.575[a]	0.23[a]	54 (R)[a]	0.41[a]	5.80 [39][b]

[a]Mechanical properties given by the distributer, Industrial Plastic Supplies ltd

[b]'Effective' work function given to dielectrics, as quoted by the literature

testing. A lower reciprocating frequency of 1 Hz was used for an additional series of tests in order to more accurately illustrate into how friction response and electronic output changed across the length of the stroke. These frequencies correlate to maximum velocities of 0.17 and 0.42 ms^{-1}, respectively. The testing procedure consisted of bringing the upper sample into contact with one lower sample at the beginning of its stroke until the desired contact force is reached. This amount of stationary contact time is kept at a constant 1 min for all tests as a way of systematically mitigating the influence of any initial stationary contact electrification when comparing test data. The two lower samples are then reciprocated back and forth at the desired frequency for 10 min, bringing each one into and out of contact with the upper sample surface in an oscillating fashion. The contact force is kept at a constant throughout this stage of testing via the force tracking and feedback loop feature of the UMT.

2.6 Data Analysis

Data from the 2D load cell, LVDT positional sensor, and both electrometers are collected and recorded by the UMT's in-built data acquisition unit; which is capable of sampling data from the five channels (x, F_x, F_z, I, and V) simultaneously up to a rate of 8 kHz. The resulting data are flagged for anomalies and cleaned, using notch filters at 50 Hz and 70 Hz to remove any external electrical and acoustic interference, respectively, before analysis using a dedicated MATLAB program. This program is also used to calculate both the energy dissipated via friction per oscillation, and the accumulation of contact charge, across the duration of a given test using the integration methods described below.

Whilst the measurement circuit is capable of directly measuring the induced flow of charge passing through it, measuring the induced conduction current over time still allows for this charge value to be calculated via integration over time. The total amount of charge being accumulated on the insulating surface across the duration of a test can be estimated by integrating the current output for each half-oscillation over time, as shown by Eq. (2). This indirect method of calculation is more favourable for macroscale applications, as measuring the contact charge directly via methods such as Kelvin probe force microscopy (KPFM, [40]) are not perfectly in situ and remain unscalable to the size of TENG applications.

$$I(t) = \frac{\mathrm{d}Q(t)}{\mathrm{d}t} \therefore Q_n = \int_{t_n}^{t_{n+1}} I(t)\mathrm{d}t \tag{2}$$

A similar method can be used to calculate the energy dissipated via friction for each forward and reverse stroke of the relative sample movement, which is a standard procedure for tribological testing. Since the work imparted by a moving object to overcome friction is treated as the integral of the resistive frictional force over the distance travelled, we can define the total energy dissipated via friction across this movement.

$$W_n^{\mathrm{fric}} = \int_{x_n}^{x_{n+1}} F_x(x)\mathrm{d}x \tag{3}$$

A time-averaged value for friction coefficient is also calculated for each forward and reverse stroke to give a clearer view of how it evolves over the duration of contact testing. The integrated nature of this value also corrects for any systematic asymmetries or fluctuations across the length of the stroke. This value is calculated as

$$\mu_n = \frac{\int_{t_n}^{t_{n+1}} F_x(t)\mathrm{d}t}{\int_{t_n}^{t_{n+1}} F_z(t)\mathrm{d}t} \tag{4}$$

3 Results and Discussion

3.1 Friction Measurements

The UMT-TENG friction output gives an insight into the tribological processes that occur within the UMT-TENG contact. Under correct interpretation, it can be used to identify the physical processes that occur within the material interface. In conjunction with the electrical output, these data can also be used to detect the presence of transfer films, third-body particles, and wear debris. The generalised form of friction response from the UMT-TENG contact remains identical between all material pairings and tribological parameters, approximating that of a square wave over time. The frequency of this wave matches that of the relative reciprocating motion of the upper and lower samples and is also in phase with the relative velocity of the upper and lower samples, as to be expected from a typical reciprocating tribometer output. A 3D depiction of the cleaned data is presented in Fig. 5a, whilst Fig. 5b shows the cleaned and raw data against sample position over a single half-oscillation.

Due to the high apparent surface area plate-on-plate nature of the UMT-TENG contact, artefacts of a high stick–slip friction regime are seen at the beginning of each stroke and reverse stroke. These artefacts take the form of high frequency oscillations in F_x and F_z, as shown in Fig. 5b, which are caused by acoustic vibrations occurring within the contact. These vibrations are caused by a difference between the static and dynamic friction coefficients for the contact, causing the surfaces to intermittently 'stick' to and 'slip' across each other [41]. This difference is known to be exhibited for almost all material pairings and manifests itself as an energy barrier, which must first be overcome if relative motion is to be initiated. Because of this

energy barrier, the static friction coefficient for any contact is normally higher than the dynamic friction coefficient for the same contact. The previously described time-averaged friction coefficient is shown to evolve over the duration of every test, indicating that tribological mechanisms cause the conditions within the contact to change dynamically over time. The presence of different mechanisms are dependent on the mechanical properties of both materials, as well as the tribological parameters that describe the form of contact. Comparisons of example friction responses from the UMT-TENG apparatus are given in Fig. 6.

3.1.1 Influence of Polymer Composition

Upon comparing the friction response of the three differing polymers, it becomes clear that they each exhibit unique tribological characteristics. The POM samples consistently exhibited the highest friction coefficient throughout testing against both stainless steel and aluminium counter-surfaces. The friction response from the POM samples show an initial high rise in friction coefficient, which gradually lessens in gradient over time. The POM samples exhibited their lowest end-of-test friction coefficient of 0.36 when polished and tested against an aluminium counter-surface. The PA66 samples exhibit the lowest friction coefficient for approximately the first minute of testing against stainless steel counter-surfaces. This friction response then gradually rises over the duration of each test up to a value between the friction coefficients of POM and PTFE. The POM samples exhibited their lowest end-of-test friction coefficient of 0.26 when tested against an aluminium counter-surface under an applied load of 5 N. The PTFE samples also exhibit this initial rise in friction coefficient. This response

generally peaks between the first 50 to 100 s of testing against stainless steel counter-surfaces but then gradually lowers over time and levels out to a value more consistent with existing friction data for PTFE contacts [42]. This lowering of friction coefficient over time may be attributed to the development of a low-friction PTFE transfer film on the counter-surface. The PTFE samples achieved the lowest friction coefficient of all three polymers for the majority of testing conditions by the end of each test. The lowest friction coefficient of 0.18 was achieved by the polished PTFE samples against stainless steel counter-surfaces under an applied load of 10 N.

3.1.2 Influence of Counter-Material

The mechanical properties of the counter-surface are shown to have a strong influence on friction response. Figure 6a, c, and e show the response of polymer samples tested against the stainless steel counter-surfaces, whereas Fig. 6b, d, and f show the response of samples tested against the aluminium counter-surfaces. Testing against the softer aluminium counter-surface yielded lower friction coefficients for POM and PA66 samples. The PTFE samples exhibited higher friction coefficients overall against aluminium. They also lacked the initial rise and fall in friction coefficient that is evident during the initial stages of tests against stainless steel. Both these trends in friction coefficient may be attributed to the relative softness of the aluminium surface in comparison to the stainless steel. The aluminium surface is more able to deform in response to applied pressure and therefore would be less abrasive on the polymer surfaces. This would ultimately lead to a lower friction coefficient for POM and PA66, but would slow down the
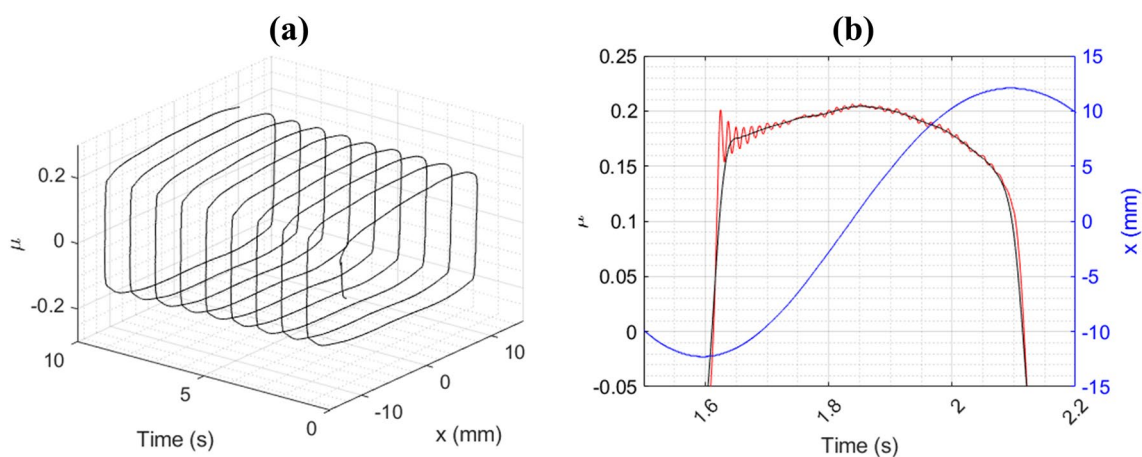

(a)

(b)

Fig. 5 a Cleaned friction coefficient against relative sample position and time for a polished PTFE on PA66 film DSF-TENG contact. b Cleaned (black) and raw (red) friction coefficient (μ) against relative sample position (blue) over time for the same contact. Samples were reciprocated at 1 Hz under an applied load of 40 N with a stroke length of 25 mm and a 2 mm lateral spacing of the lower samples. The apparent area of the contact is 23 mm by 50 mm.
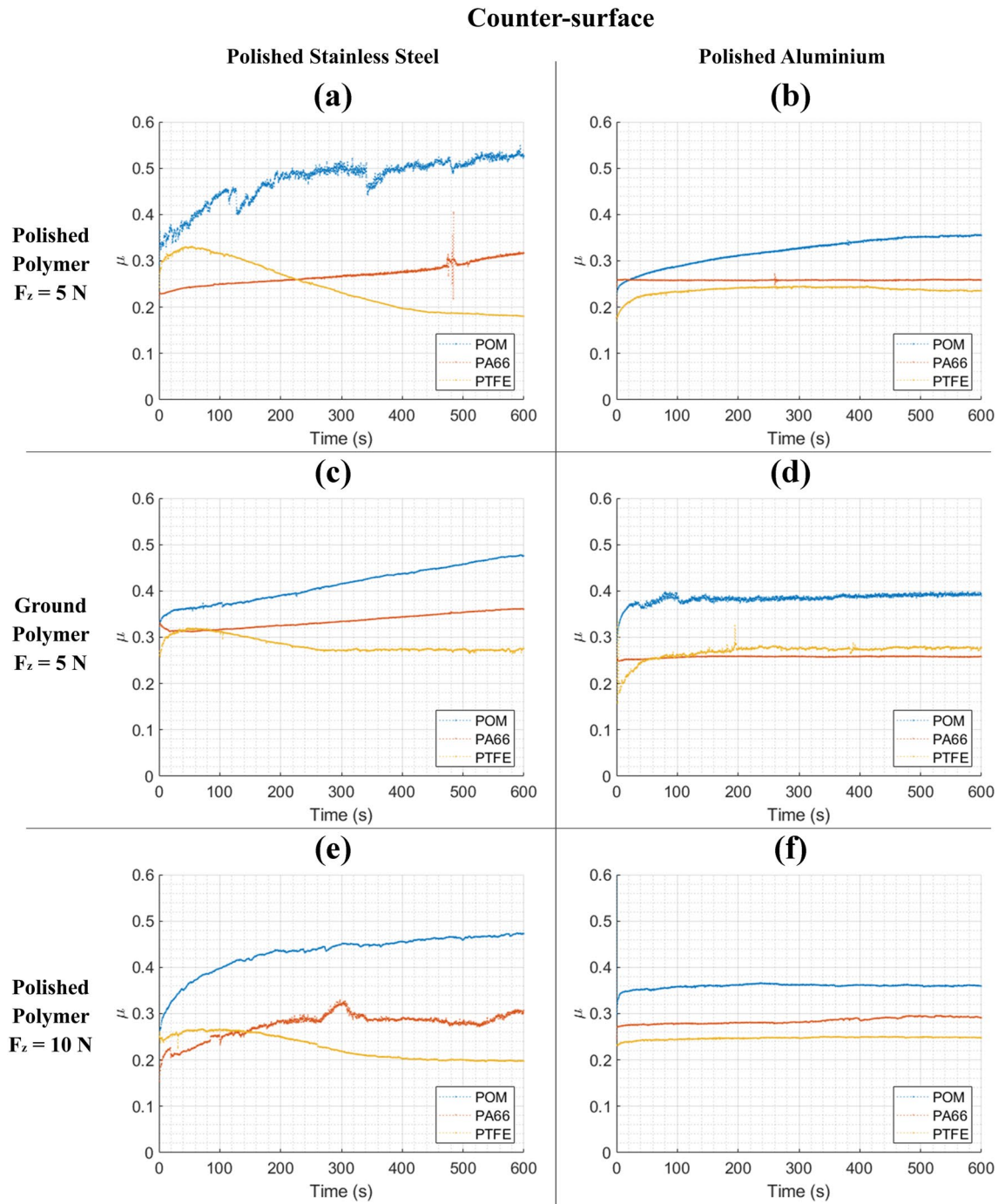
Counter-surface

Fig. 6 Friction coefficient over time for **a** polished polymers on polished stainless steel DSF-TENG contacts under an applied load of 5 N, **b** polished polymers on polished aluminium DSF-TENG contacts under an applied load of 5 N, **c** ground polymers on polished stainless steel DSF-TENG contacts under an applied load of 5 N, **d** ground polymers on polished aluminium DSF-TENG contacts under an applied load of 5 N, **e** polished polymers on polished stainless steel DSF-TENG contacts under an applied load of 10 N, **f** polished polymers on polished aluminium DSF-TENG contacts under an applied load of 10 N. Samples were reciprocated at 2.5 Hz with a stroke length of 25 mm and a 2 mm lateral spacing of the lower samples. The apparent area of the contact is 23 mm by 50 mm when the upper sample fully encompasses a lower sample

process of PTFE transfer film formation since less material would be removed from the PTFE surface.

3.1.3 Influence of Surface Roughness

Upon comparing the response of differing roughness parameters for otherwise identical polymers, it becomes clear that the roughness of the polymer samples also influences the friction response and how it evolves over time. Figure 6a and b show the response of polished polymer samples under an applied load of 5 N, whereas Fig. 6c and d show the response of samples that had been ground using 180 grit SiC pads prior to testing. For POM, the polished samples exhibited a higher friction coefficient up to a value of 0.52 after 10 min of testing, whereas the friction coefficient for the ground samples after 10 min of testing was 0.47. This may be attributed to an increased adhesion between the two more conformal surfaces. The polished PA66 samples generally exhibited a lower friction coefficient than the ground ones across testing. The ground, PA66 surfaces also exhibit an initial drop in friction coefficient prior to this steady rise. This initial high friction coefficient and subsequent drop is an indicator of abrasive wear, as it truncates the surface profile of the PA66 samples to one which conforms better to the harder metal counter-surface. Both the polished and ground PTFE topographies peaked at approximately the same time and friction coefficient. However, the polished PTFE samples gave substantially lower and more stable friction responses after this point, giving steady state μ values of ~0.18 as opposed to ~0.27 for the ground samples.

3.1.4 Influence of Applied Load

Friction coefficients remained similar for most material pairings under higher applied loads. Figure 6a and b, show the response of polished polymer samples tested under an applied load of 5 N, whereas Fig. 6e and f show the response of identical samples tested under an applied load of 10 N. The friction coefficients for the POM contacts reach similar values, but reach those values at a faster rate, which is best shown against the aluminium counter-surfaces. The PA66 samples exhibited higher and less stable friction responses under the higher applied load, with these instabilities in friction response indicating the removal of material from the contact. The PTFE samples reached a similar friction coefficient under higher loads. Similarly to the POM samples, the PTFE samples reached these values at a faster rate. In addition the characteristic initial rise and fall in friction coefficient is lessened in magnitude when tested under higher loads against the stainless steel counter-surface.

3.1.5 Wear Analysis

An important factor to consider with regards to the application and use of polymers within a tribological contact is that polymers often exhibit low mechanical moduli [43]. This in turn may lead to significant material wear within polymer contacts, most notably against harder counter-surfaces [44]. The unfortunate phenomenon that accompanies higher applied loads in dry friction is an increase in these material wear rates [45]. The polymer samples used in testing were analysed using a using a Bruker NPFLEX white-light interferometer to accurately measure their roughness parameters before and after tribological testing. These parameters were measured from 3D surface topography maps taken across 3 separate 500 μm by 500 μm sample areas per sample surface and are displayed in Table 2. Evidence of material removal is evident on all post-tested polymer surfaces through distinct changes in their topographies. Evidence of abrasive wear along the axis of reciprocation is seen on the polished polymer samples, leading to a significant increase in their mean arithmetic roughness's (R_a). An example of these changes in topography is given in Fig. 7a and b. The ground samples exhibit lower rms slope (R_{dq}) values after tribological testing, despite similar R_a values, which imply a profile truncation caused by the removal of asperities. Both PA66 and POM are known to exhibit relatively high mechanical moduli in comparison to PTFE [46] and thus exhibit less severe signs of material wear.

The polymer samples were also analysed using attenuated total reflection fourier-transform infrared spectroscopy (ATR-FTIR) before and after tribological testing as a way of gauging any potential changes in surface composition. The

Table 2 Surface topography parameters for all sample surfaces used in UMT-TENG testing

Material	R_a (nm)	R_{dq}	R_{sk}	R_{ku}
Stainless steel (polished)	11	0.008	−2.5	18.1
Aluminium (polished)	5	0.004	−3.3	55
Delrin (polished)	260	0.17	−0.6	3.7
Nylon 6-6 (polished)	290	0.17	−0.2	3.4
Teflon (polished)	170	0.09	−0.5	3.9
Delrin (180 grit)	1700	0.57	−0.7	4.3
Nylon 6-6 (180 grit)	1900	0.67	−0.3	4.4
Teflon (180 grit)	1500	0.48	0.1	3.1
Delrin (Polished, Worn)	2000	0.47	1.4	9.9
Nylon 6-6 (Polished, Worn)	1500	0.31	−1.9	11.4
Teflon (Polished, Worn)	1200	0.27	−1.2	5.4
Delrin (180 grit, worn)	3500	0.32	−0.4	2.1
Nylon 6-6 (180 grit, Worn)	2400	0.36	−1.2	6.9
Teflon (180 grit, Worn)	1300	0.38	0.6	4.4

wear debris from any test that produced a sufficient amount was also analysed in a similar fashion. The composition of the aforementioned transfer films, generated by testing PTFE samples against both metal counter-surfaces, is confirmed to be PTFE under FTIR analysis as shown in Fig. 7d. Wear debris was also observed from POM samples against aluminium

Fig. 7 **a** Example topography of unworn polished PTFE sample. **b** Example topography of worn PTFE sample. **c** Example topography of PTFE wear debris on a stainless steel counter-surface after contact testing against PTFE, measured using a Bruker NPFLEX white-light interferometer. **d** ATR-FTIR spectra of the PTFE surface prior to testing (blue) and the observed transfer film (orange). **e** Example topography of wear debris on an aluminium counter-surface after contact testing against POM, measured using a Bruker NPFLEX white-light interferometer. **f** ATR-FTIR spectra of the POM surface prior to testing (blue) and the observed wear debris (orange). **g** Example topography of embedded wear debris on a PA66 surface after contact testing against Aluminium (Color figure online).
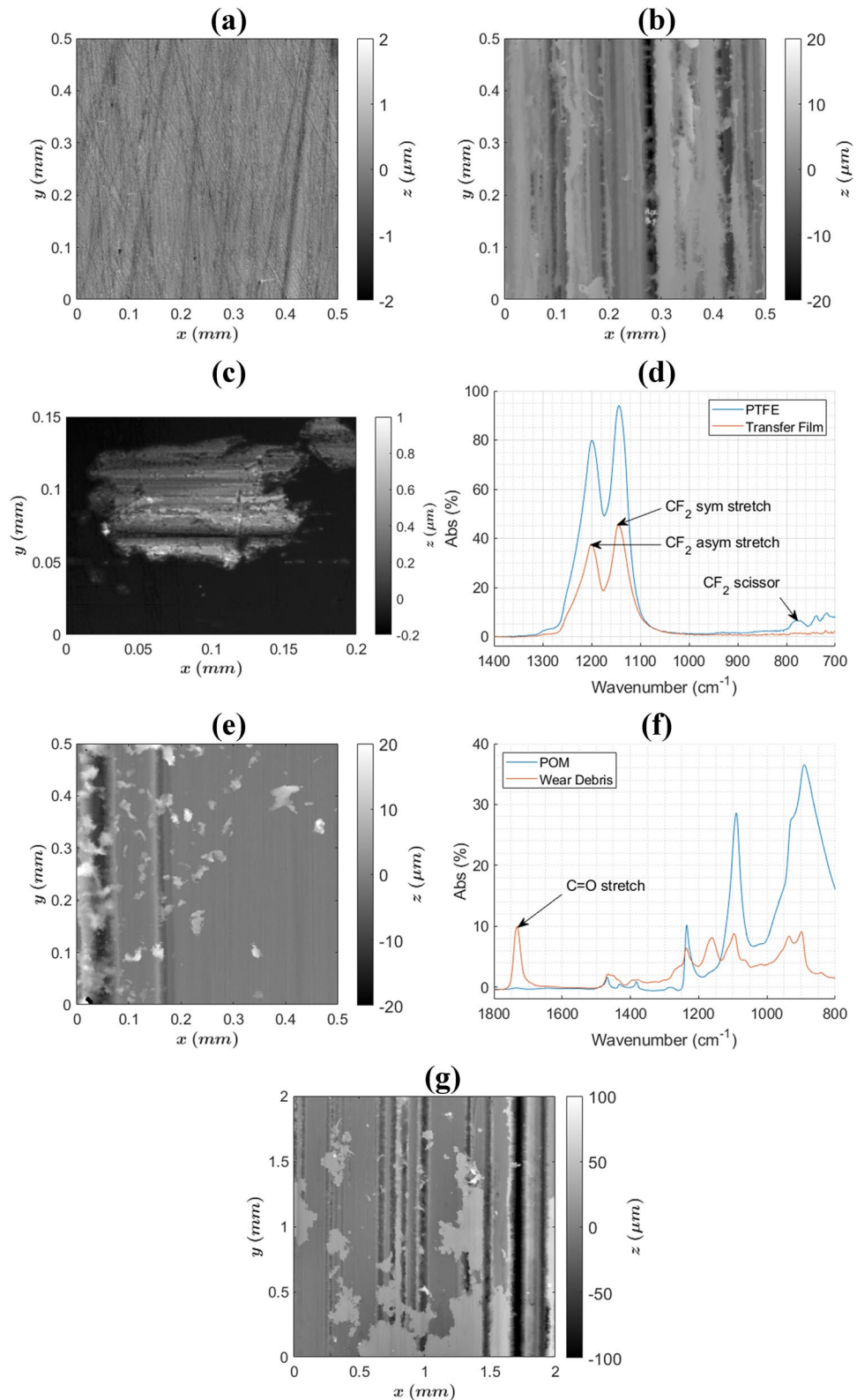
counter-surfaces under an applied load of 10 N, but not against stainless steel. The composition of this wear debris was also different to that of POM, which is confirmed via ATR-FTIR in Fig. 7f. One identifiable and prominent feature of this FTIR spectra is a sharp peak at 1730 cm^{-1}, indicating the presence of ester groups within the wear debris [46]. The Nylon samples deposited very little wear debris onto any counter-surface, however an amount of wear debris was instead observed to become embedded into the Nylon surface under higher loads as shown in Fig. 7g.

3.2 Electronic Output Measurements

3D depictions of a typical voltage and current response from high and low-impedance UMT-TENG contact tests are, respectively, given in Fig. 8a and b. Simultaneous measurements of output voltage and current over a given external load are also given in Fig. 8c and d. Upon Measurement of the electronic output properties of the UMT-TENG contact under open-circuit, short-circuit, and finite impedance measurement modes, alternating voltage and current traces are observed. Under high-impedance measurements ($\gtrsim$ 1 GΩ) the voltage trace accurately reflects the movement of mirror charges across the measurement circuit to correlate with the upper sample position, as shown in Fig. 8a and c. The current trace at such high impedances reflects the capacitive reactance of the TENG device; being proportional to the time differential of the voltage trace and therefore dependant on the relative velocity of the upper and lower samples, as shown in Fig. 8b and c. At lower impedances ($\lesssim$ 10 MΩ) the device output is shown to be ohmic, where the voltage trace is equal to the current trace multiplied by the resistive impedance of the external measurement circuit as shown in Fig. 8d. This confirms that the measured current trace is the free movement of mirror charges
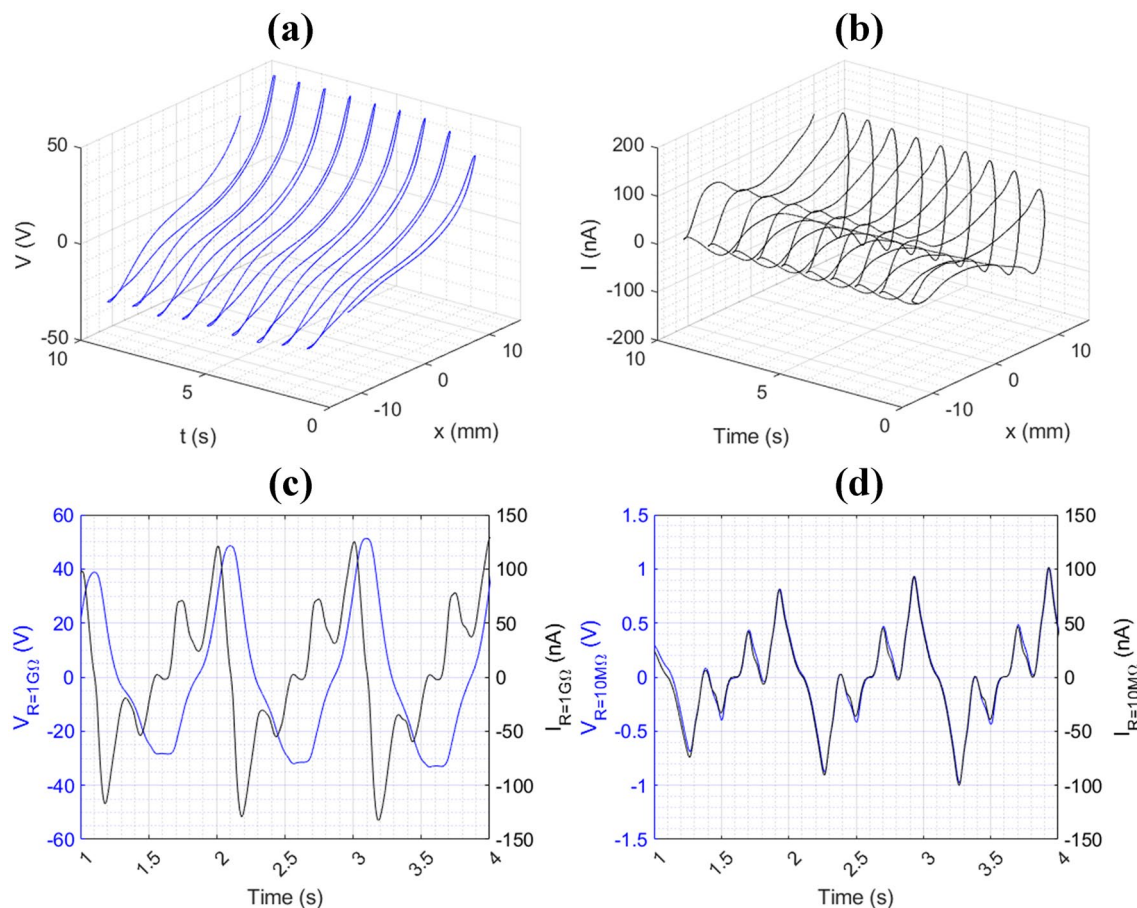

Fig. 8 **a** Output voltage against relative sample position and time for a polished PTFE on PA66 film DSF-TENG contact under an external resistance of approximately > 2e^{14} Ω (the input resistances of the two 6517B electrometers in series). **b** Output current against relative sample position and time for an identical contact under an external resistance of ≪ 1 Ω (6517B connected as an ammeter with negligible voltage burden). **c** Output voltage (blue) and current (black) over time for an identical contact under an external resistance of 1 GΩ. **d** Output voltage (blue) and current (black) over time for an identical contact under an external resistance of 10 MΩ. Samples were reciprocated at 1 Hz under an applied load of 40 N with a stroke length of 25 mm and a 2 mm lateral spacing of the lower samples. The apparent area of the contact is 23 mm by 50 mm (Color figure online).

between the lower samples to accommodate for the change in local electric field, caused by the physical movement of the charged upper sample surface. The magnitude and polarity of the tribocharges on the upper sample surface also influence the polarity and magnitude of the current output.

3.3 Contact Charge Accumulation

The current output from each forward and reverse stroke across the duration of each test is integrated over time as described by Eq. (2). This returns the total amount of charge that has passed through the ammeter during each movement, and thus gives an estimation of the total amount of tribocharges retained on the polymer surface. Analysis of contact charge over time for each material pairing firstly reveals its transient nature. An initial stage of charge accumulation is shown to occur when previously uncharged and dissimilar surfaces are brought into contact. The exact formulation of how electrostatic charge accumulates within tribological contacts is the subject of further discussion. Previous research has concluded that an exponential model for charge accumulation fits well for contacts that have negligible changes in real contact area or pressure [23]. The maximum charge density, as well as the rate at which this charge accumulation occurs, is shown to be dependent on both material pairing and contact topography. These relationships are depicted in Fig. 9 in the same layout as previously described for Fig. 6.

3.3.1 Influence of Polymer Composition

It is known that some polymers are known to generally accumulate surface electrons when in contact with other materials by having low-energy unoccupied molecular orbitals [18], whereas some polymers generally donate electrons to their respective counter-surfaces from high-energy occupied states [47]. PTFE has seen much use as an electronegative material choice in TENG contacts owing to its exceptional performance as an electron acceptor [48]. PA66 and POM are two polymers that have been proven in literature to donate electrons to most counter-surfaces [2]. PA66 in particular has seen extensive use in TENG contacts as an electropositive contact-surface [49]. The PTFE surfaces all accumulated a negative charge throughout the initial stages of contact testing, indicating the acceptance of electrons from both the aluminium and stainless steel counter-surfaces as predicted. The POM and PA66 surfaces all accumulated a positive charge during the initial stages of contact testing, indicating the donation of electrons to both the aluminium and stainless steel counter-surfaces, also in accordance with previous literature [2]. The POM samples were shown to accumulate the highest magnitude of charge against stainless steel counter-surfaces, whereas the PTFE samples accumulated the highest magnitude of charge against the aluminium counter-surfaces. These data indicate that the

work functions of both metal surfaces lie between the 'effective' work functions of PTFE and PA66 due to the polarity of the charges being accumulated on the polymer surfaces.

3.3.2 Influence of Counter-Material

The composition of the conductive counter-surface was shown to have an influence on the magnitude and polarity of charges being transferred via triboelectric charging. Both the POM and PA66 surfaces accumulated less charge against aluminium than against stainless steel, whereas the PTFE surfaces accumulated more charge against aluminium. The polished POM samples are shown to accumulate a greater amount of charge than the polished PA66 samples, whereas this is reversed when the samples are tested against aluminium surfaces. This indicates that the 'effective' work function for POM is lower than that of PA66, meaning that the highest occupied molecular orbital for POM is likely to be at a higher energy than that of PA66. These data also indicate that the work function of the aluminium counter-surfaces is lower than that of the stainless steel counter-surfaces. Both metals are known to produce passive oxide surface layers, in the order of several nm thick, due to the high reactivity of their exposed metallic surfaces. The oxide layers that form on stainless steel surfaces however are mostly composed of iron oxides, molybdenum oxides and chromium oxides due to the composition of the alloy [48, 49].

3.3.3 Influence of Surface Roughness

Previous research has suggested that increasing the real contact area of a TENG contact increases the total surface area through which triboelectric charging can occur [23]. Ultimately this implies that two smooth and conformal surfaces should accumulate a greater amount of charge via triboelectric charging than two, otherwise identical, non-conformal surfaces. The ground POM and PA66 surfaces are shown to accumulate more charge against aluminium counter-surfaces than their polished equivalents, which can also be said for the PTFE samples being tested against stainless steel. However, for the remaining material pairings the ground surfaces accumulated a greater charge than their polished counterparts. This implies that there are more complex processes occurring within the TENG contact that affect triboelectric charging.

3.3.4 Influence of Applied Load

Increasing the applied load to the UMT-TENG contact is shown to increase both the rate of charge accumulation and the saturation charge density within it for all material pairings. Extensive tribological research has previously concluded that increasing the applied load to a typical mechanical contact increases the proportional area of real contact within the
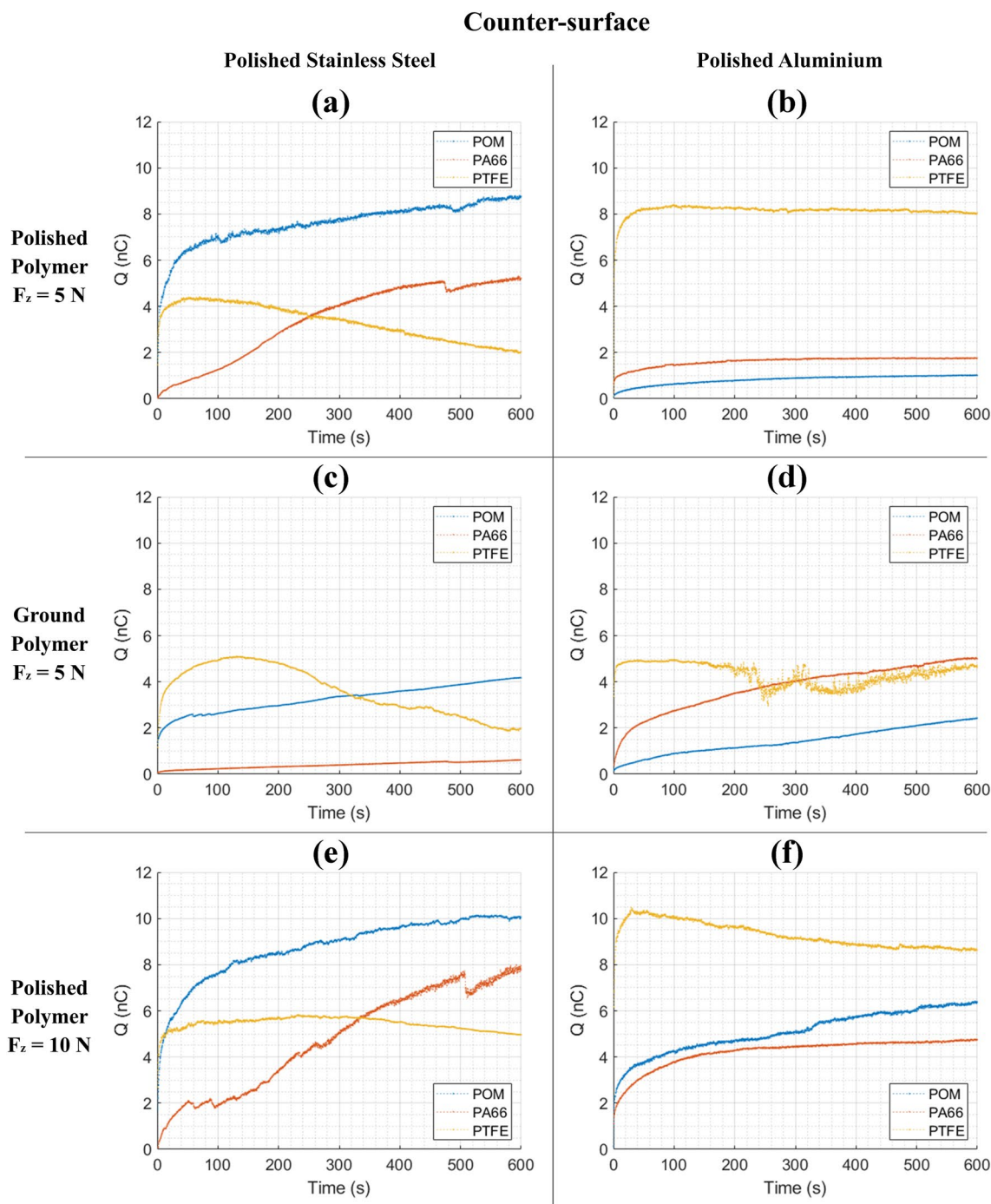
Counter-surface

Fig. 9 Contact charge over time for **a** polished polymers on polished stainless steel DSF-TENG contacts under an applied load of 5 N, **b** polished polymers on polished aluminium DSF-TENG contacts under an applied load of 5 N, **c** ground polymers on polished stainless steel DSF-TENG contacts under an applied load of 5 N, **d** ground polymers on polished aluminium DSF-TENG contacts under an applied load of 5 N, **e** polished polymers on polished stainless steel DSF- TENG contacts under an applied load of 10 N, **f** polished polymers on polished aluminium DSF-TENG contacts under an applied load of 10 N. Samples were reciprocated at 2.5 Hz with a stroke length of 25 mm and a 2 mm lateral spacing of the lower samples. The apparent area of the contact is 23 mm by 50 mm when the upper sample fully encompasses a lower sample

apparent area of contact [50]. Whilst this increase in real contact area may contribute to triboelectric charging, as explained previously, it is also possible that the increase in energy dissipated into the contact via friction may enhance triboelectric charging through phonon-electron interactions [28].

3.4 Comparison of Tribological and Electronic Measurement Results

The ability to simultaneously measure both the friction response and electrical output of the UMT-TENG contact gives an insight into how tribology influences triboelectric charging within it. Contact testing reveals that the amount of charge accumulated within the UMT-TENG contact, as well as the rates at which this charge accumulates and dissipates, is dependent on a multitude of tribological processes, in addition to the difference in surface electronic structures.

For PTFE contacts, a maximum charge density is reached within the first few minutes of contact testing. After this point, the charge within the contact then begins to diminish. The data presented in Figs. 6 and 9 indicate that the amount of electrostatic charge trapped within the contact diminishes in a similar fashion to the friction coefficient over the duration of testing. This reduction in contact charge could therefore attributed to the PTFE transfer film formation within the contact. During transfer film formation, PTFE wear particles are removed from the bulk material and deposited on the counter-surface. Further triboelectric charge transfer is inhibited in these areas due to the contact potential difference between the PTFE surface and the newly formed PTFE transfer film becoming substantially smaller than the CPD between the PTFE and the previously exposed counter-surface. Previously accumulated triboelectric charges on the PTFE surface may also be removed through contact with the PTFE transfer film on the counter-surface via tribo 'de-electrification' between the similar materials [16]. The formation of PTFE transfer films is beneficial in some circumstances where a self-replenishing solid lubricant is needed. PTFE transfer films in particular are known to lower the friction coefficient within contacts [40] by covering any asperities to reduce abrasive wear, in addition to reducing adhesive forces between the PTFE surface and the newly generated PTFE counter-surface. This tribological behaviour can be explained by the loosely bonded rod-like molecular structure of PTFE [51]. This friction behaviour, explained by the development of a low-friction transfer film, is seen to progress more expediently when tested against the harder stainless steel counter-surface. This behaviour is also reflected in the electronic output, where the contact charge diminishes more noticeably over time against the stainless steel counter-surfaces. These data combined indicate that a PTFE transfer film is slower to develop across the aluminium counter-surfaces under the same contact force and relative motion.

This similarity between friction coefficient and contact charge continues for both POM and PA66 contacts, where an increasing friction coefficient over time is followed by an increase in contact charge. The exact underlying mechanisms behind this relationship are in need of further investigation. It is plausible that an increase in contact charge is caused by electron excitation, via phonons created by friction and material deformation [28]. Research also suggests that 'coulomb adhesion' caused by the electrostatic attraction of the charged contacting surfaces may increase the friction coefficient between them [52]. Abrupt reductions in contact charge are also occasionally observed during contact testing, which coincide with an associated change in friction coefficient. These combined phenomena indicate the removal of charged material from the contact. An example of this can be seen in Figs. 6a and 9a where the PA66 sample exhibits an abrupt lowering of contact charge associated with fluctuations in friction coefficient.

4 Summary

In this work, an effective methodology for investigating the tribological properties of TENG devices is presented. This methodology comprises of a reciprocating tribometer, modified to accommodate and test under varying tribological conditions most laterally sliding TENG device constructions. Both the friction response and electrical output are measured in situ whilst the applied load and reciprocating frequency is controlled. The apparatus is capable of testing under contact forces between 0.5 and 50 N and at reciprocating frequencies of up to 10 Hz at a stroke length of 25 mm. The newly assembled electronic measurement circuit is capable of simultaneous voltage and current measurements at varying external load resistances, with a time resolution as low as 0.125 ms. Through the implementation of this methodology, the generation of electrostatic charge within the TENG device is accurately measured in situ.

5 Conclusion

The following conclusions are drawn from this work:

- Tribology plays an important role in the triboelectric charging processes in TENG. In particular, we have shown that friction coefficient and shear stresses are directly affecting the charge transfer.
- Both surface electronic structure and contact topography influence the rate at which triboelectric charge is generated within a contact, as well as the maximum saturation charge density of said contact.
- Increasing the applied load enhances the mechanism of triboelectric charging, which could be attributed to the

increased area of contact and/or increased shear stresses within this area of contact.

- Tribological tests conclude that material wear plays a significant part in the breakdown of accumulated charge within a TENG contact. This mechanism is most prominently exhibited by the formation of PTFE transfer films when PTFE surfaces are tested against a harder counter-surface.
- To the best of our knowledge, this is the first time that the effect of material degradation on the TENG performance is investigated. This highlights the needs for more comprehensive studies on the effect of wear of the performance of TENG in order to be able to design, manufacture and maintain durable TENGs.

Data Availability The data associated with this paper is available from University of Leeds at https://doi.org/10.5518/1118.

Declarations

Competing Interests All authors declare they have no financial or non-financial interests.

References

1. Wang, Z.L., Wang, A.C.: On the origin of contact-electrification. Mater. Today (2019). https://doi.org/10.1016/J.MATTOD.2019.05.016

2. Diaz, A.F., Felix-Navarro, R.M.: A semi-quantitative tribo-electric series for polymeric materials: the influence of chemical structure and properties. J. Electrostat. **62**, 277–290 (2004). https://doi.org/10.1016/J.ELSTAT.2004.05.005

3. Kwak, S.S., Lin, S., Lee, J.H., Ryu, H., Kim, T.Y., Zhong, H., et al.: Triboelectric charging-induced large electric power generation from a single moving droplet on graphene/polytetrafluoroethylene. ACS Nano **10**, 7297–7302 (2016). https://doi.org/10.1021/acsnano.6b03032

4. Matsusaka, S., Masuda, H.: Electrostatics of particles. Adv. Powder Technol. **14**, 143–166 (2003). https://doi.org/10.1163/156855203763593958

5. Šupuk, E., Zarrebini, A., Reddy, J.P., Hughes, H., Leane, M.M., Tobyn, M.J., et al.: Tribo-electrification of active pharmaceutical ingredients and excipients. Powder Technol. **217**, 427–434 (2012). https://doi.org/10.1016/J.POWTEC.2011.10.059

6. Kiss, I., Szedenik, N., Berta, I.: Electrostatic hazard and protection: expert system for fuel delivery modules. J. Electrostat. **63**, 495–499 (2005). https://doi.org/10.1016/j.elstat.2005.03.008

7. Yadav, R., Tirumali, M., Wang, X., Naebe, M., Kandasubramanian, B.: Polymer composite for antistatic application in aerospace. Def. Technol. **16**, 107–118 (2020). https://doi.org/10.1016/j.dt.2019.04.008

8. Wang, Z.L., Jiang, T., Xu, L.: Toward the blue energy dream by triboelectric nanogenerator networks. Nano Energy **39**, 9–23 (2017). https://doi.org/10.1016/J.NANOEN.2017.06.035

9. Wang, Z.L.: On Maxwell's displacement current for energy and sensors: the origin of nanogenerators. Mater. Today **20**, 74–82 (2017). https://doi.org/10.1016/J.MATTOD.2016.12.001

10. Fan, F.-R., Tian, Z.-Q., Lin, W.Z.: Flexible triboelectric generator. Nano Energy **1**, 328–334 (2012). https://doi.org/10.1016/J.NANOEN.2012.01.004

11. Zhu, G., Peng, B., Chen, J., Jing, Q., Lin, W.Z.: Triboelectric nanogenerators as a new energy technology: from fundamentals, devices, to applications. Nano Energy **14**, 126–138 (2015). https://doi.org/10.1016/J.NANOEN.2014.11.050

12. Chen, J., Wang, Z.L.: Reviving vibration energy harvesting and self-powered sensing by a triboelectric nanogenerator. Joule **1**, 480–521 (2017). https://doi.org/10.1016/J.JOULE.2017.09.004

13. Wang, S., Lin, L., Wang, Z.L.: Triboelectric nanogenerators as self-powered active sensors. Nano Energy **11**, 436–462 (2015). https://doi.org/10.1016/J.NANOEN.2014.10.034

14. Xu, C., Zi, Y., Wang, A.C., Zou, H., Dai, Y., He, X., et al.: On the Electron-Transfer Mechanism in the Contact-Electrification Effect. Adv Mater **30**, 1706790 (2018). https://doi.org/10.1002/adma.201706790

15. Lee, L.-H.: Dual mechanism for metal-polymer contact electrification. J Electrostat **32**, 1–29 (1994). https://doi.org/10.1016/0304-3886(94)90026-4

16. Soh, S., Kwok, S.W., Liu, H., Whitesides, G.M.: Contact de-electrification of electrostatically charged polymers. J. Am. Chem. Soc. **134**, 20151–20159 (2012). https://doi.org/10.1021/ja309268n

17. Fabish, T.J., Duke, C.B.: Molecular charge states and contact charge exchange in polymers. J. Appl. Phys. **48**, 4256–4266 (1977). https://doi.org/10.1063/1.323412

18. Shirakawa, Y., Ii, N., Yoshida, M., Takashima, R., Shimosaka, A., Hidaka, J.: Quantum chemical calculation of electron transfer at metal/polymer interfaces. Adv. Powder Technol. **21**, 500–505 (2010). https://doi.org/10.1016/j.apt.2010.05.007

19. Kahn, A.: Fermi level, work function and vacuum level. Mater. Horizons **3**, 7–10 (2016). https://doi.org/10.1039/c5mh00160a

20. Matsusaka, S., Maruyama, H., Matsuyama, T., Ghadiri, M.: Triboelectric charging of powders: a review. Chem. Eng. Sci. **65**, 5781–5807 (2010). https://doi.org/10.1016/J.CES.2010.07.005

21. Sato, T., Koswattage, K.R., Nakayama, Y., Ishii, H.: Density of states evaluation of an insulating polymer by high-sensitivity ultraviolet photoemission spectroscopy. Appl. Phys. Lett. **110**, 111102 (2017). https://doi.org/10.1063/1.4978529

22. Zhou, Y.S., Liu, Y., Zhu, G., Lin, Z.-H., Pan, C., Jing, Q., et al.: In situ quantitative study of nanoscale triboelectric charging and patterning. Nano Lett. **13**, 2771–2776 (2013). https://doi.org/10.1021/nl401006x

23. Armitage, J.L., Ghanbarzadeh, A., Wang, C., Neville, A.: An investigation into the influence of tribological parameters on the operation of sliding triboelectric nanogenerators. Tribol. Int. **155**, 106778 (2021). https://doi.org/10.1016/j.triboint.2020.106778

24. Yang, J., Yang, F., Zhao, L., Shang, W., Qin, H., Wang, S., et al.: Managing and optimizing the output performances of a triboelectric nanogenerator by a self-powered electrostatic vibrator switch. Nano Energy **46**, 220–228 (2018). https://doi.org/10.1016/j.nanoen.2018.02.013

25. Niu, S.: Theoretical systems of triboelectric nanogenerators. Nano Energy **14**, 161–192 (2015). https://doi.org/10.1016/J.NANOEN.2014.11.034

26. Niu, S., Liu, Y., Wang, S., Lin, L., Zhou, Y.S., Hu, Y., et al.: Theory of sliding-mode triboelectric nanogenerators. Adv. Mater. **25**, 6184–6193 (2013). https://doi.org/10.1002/adma.201302808

27. Kim, T., Kim, D.Y., Yun, J., Kim, B., Lee, S.H., Kim, D., et al.: Direct-current triboelectric nanogenerator via water electrification and phase control. Nano Energy **52**, 95–104 (2018). https://doi.org/10.1016/J.NANOEN.2018.07.048

28. Pan, S., Zhang, Z.: Triboelectric effect: a new perspective on electron transfer process. J Appl Phys **122**, 144302 (2017). https://doi.org/10.1063/1.5006634

29. Hu, R., Krylov, S.Y., Frenken, J.W.M.: On the origin of frictional energy dissipation. Tribol. Lett. **68**, 1–13 (2020). https://doi.org/10.1007/S11249-019-1247-7/FIGURES/7

30. Min, G., Xu, Y., Cochran, P., Gadegaard, N., Mulvihill, D.M., Dahiya, R.: Origin of the contact force-dependent response of triboelectric nanogenerators. Nano Energy **83**, 105829 (2021). https://doi.org/10.1016/J.NANOEN.2021.105829

31. Zhang, W., Gu, G., Shang, W., Luo, H., Wang, T., Zhang, B., et al.: A general charge compensation strategy for calibrating the voltage of a triboelectric nanogenerator measured by a capacitive circuit. Nano Energy **86**, 106056 (2021). https://doi.org/10.1016/J.NANOEN.2021.106056

32. Zhang, W., Gu, G., Qin, H., Li, S., Shang, W., Wang, T., et al.: Measuring the actual voltage of a triboelectric nanogenerator using the non-grounded method. Nano Energy **77**, 105108 (2020). https://doi.org/10.1016/J.NANOEN.2020.105108

33. Dharmasena, R.D.I.G., Jayawardena, K.D.G.I., Mills, C.A., Deane, J.H.B., Anguita, J.V., Dorey, R.A., et al.: Triboelectric nanogenerators: providing a fundamental framework. Energy Environ. Sci. **10**, 1801–1811 (2017). https://doi.org/10.1039/c7ee01139c

34. Eastment, R.M., Mee, C.H.B.: Work function measurements on (100), (110) and (111) surfaces of aluminium. J. Phys. F **3**, 1738 (1973). https://doi.org/10.1088/0305-4608/3/9/016

35. Barrett, N., Renault, O., Lemaître, H., Bonnaillie, P., Barcelo, F., Miserque, F., et al.: Microscopic work function anisotropy and surface chemistry of 316L stainless steel using photoelectron emission microscopy. J. Electron Spectrosc. Relat. Phenom. **195**, 117–124 (2014). https://doi.org/10.1016/J.ELSPEC.2014.05.015

36. Peckner, D., Bernstein, I.M.: Handbook of Stainless Steels. McGraw-Hill Book Company, New York (1977)

37. ASM Handbook Committee. ASM Handbook Volume 2: Properties and Selection: Nonferrous Alloys and Special-Purpose Materials. 10th ed. ASM International (1990)

38. Arridge, R.G.C.: The static electrification of nylon 66. Br. J. Appl. Phys. **18**, 1311–1316 (1967). https://doi.org/10.1088/0508-3443/18/9/314

39. Trigwell, S., Grable, N., Yurteri, C.U., Sharma, R., Mazumder, M.K.: Effects of surface properties on the tribocharging characteristics of polymer powder as applied to industrial processes. IEEE Trans. Ind. Appl. **39**, 79–86 (2003). https://doi.org/10.1109/TIA.2002.807228

40. Melitz, W., Shen, J., Kummel, A.C., Lee, S.: Kelvin probe force microscopy and its application. Surf. Sci. Rep. **66**, 1–27 (2011). https://doi.org/10.1016/J.SURFREP.2010.10.001

41. Viswanathan, K., Sundaram, N.K.: Distinct stick-slip modes in adhesive polymer interfaces. Wear **376–377**, 1271–1278 (2017). https://doi.org/10.1016/J.WEAR.2016.12.017

42. Biswas, S.K., Vijayan, K.: Friction and wear of PTFE—a review. Wear **158**, 193–211 (1992). https://doi.org/10.1016/0043-1648(92)90039-B

43. Crawford, R.J., Martin, P.J.: Mechanical behaviour of plastics. In: Plastics Engineering, pp. 59–194 (2020). https://doi.org/10.1016/B978-0-08-100709-9.00002-9.

44. Briscoe, B.J., Sinha, S.K.: Wear of polymers. Proc. Inst. Mech. Eng. J **216**, 401–413 (2002). https://doi.org/10.1243/135065002762355325

45. Dangnan, F., Espejo, C., Liskiewicz, T., Gester, M., Neville, A.: Friction and wear of additive manufactured polymers in dry contact. J. Manuf. Process. **59**, 238–247 (2020). https://doi.org/10.1016/j.jmapro.2020.09.051

46. Kuptsov, A.H., Zhizhin, G.N.: Handbook of Fourier Transform Raman and Infrared Spectra of Polymers (1998)

47. Zhou, Y., Deng, W., Xu, J., Chen, J.: Engineering materials at the nanoscale for triboelectric nanogenerators. Cell Rep. Phys. Sci. **1**, 100142 (2020). https://doi.org/10.1016/J.XCRP.2020.100142

48. Chen, X., Zhao, A., Li, J., Deng, J., Zhang, G., Zhao, X.: First-principle investigation of the charge injection barriers of polyethylene and polytetrafluoroethylene oligomers. J. Appl. Phys. **126**, 035101 (2019). https://doi.org/10.1063/1.5089863

49. Wang, S., Lin, L., Xie, Y., Jing, Q., Niu, S., Wang, Z.L.: Sliding-triboelectric nanogenerators based on in-plane charge-separation mechanism. Nano Lett. **13**, 2226–2233 (2013). https://doi.org/10.1021/nl400738p

50. Xu, Y., Min, G., Gadegaard, N., Dahiya, R., Mulvihill, D.M.: A unified contact force-dependent model for triboelectric nanogenerators accounting for surface roughness. Nano Energy **76**, 105067 (2020). https://doi.org/10.1016/j.nanoen.2020.105067

51. Holt, D.B., Farmer, B.L., Macturk, K.S., Eby, R.K.: Fluoropolymer force fields derived from semiempirical molecular orbital calculations. Polymer (Guildf) **37**, 1847–1855 (1996). https://doi.org/10.1016/0032-3861(96)87301-0

52. Luo, N., Feng, Y., Zhang, L., Sun, W., Wang, D., Sun, X., et al.: Controlling the tribological behavior at the friction interface by regulating the triboelectric charging. Nano Energy **87**, 106183 (2021). https://doi.org/10.1016/J.NANOEN.2021.106183